

Unravelling the structure and strength of the highest boride of tungsten WB_{4.2}

Weiguang Gong,¹ Chang Liu,¹ Xianqi Song,¹ Quan Li,^{1,2,*} Yanming Ma,^{1,2} and Changfeng Chen^{1,3,†}

¹State Key Laboratory of Superhard Materials, Key Laboratory of Automobile Materials of MOE, Department of Materials Science, and Innovation Center for Computational Physics Method and Software, Jilin University, Changchun 130012, China

²International Center of Future Science, Jilin University, Changchun 130012, China

³Department of Physics and Astronomy, University of Nevada, Las Vegas, Nevada 89154, USA



(Received 29 May 2019; revised manuscript received 26 November 2019; published 17 December 2019)

Tungsten tetraboride is outstanding among transition-metal light-element compounds for its easy synthesis and superior mechanical properties. Its crystal structure, however, has eluded scientists for over half a century, impeding fundamental understanding and rational property optimization. Recent x-ray and neutron diffraction studies suggest rare boron trimers occupying vacant metal sites in the highest boride of tungsten WB_{4.2}, but a viable crystal structure and key mechanical properties remain unresolved. Here we identify a WB_{4.2} phase in orthorhombic symmetry with a very large 104-atom unit cell using a tailored search algorithm treating boron trimer as a coherent unit. First-principles studies establish phase stability and unveil the mechanism for strength enhancement by newly identified bonding features. These findings solve a challenging crystal structure and elucidate its benchmark mechanical behaviors. This work offers powerful insights for exploring novel structures and properties of materials containing intricate multiaatomic constituent structural units.

DOI: 10.1103/PhysRevB.100.220102

Transition-metal light-element (TM-LE) compounds have been the intense focus of recent research in the broad interdisciplinary fields of physics, chemistry, and materials science. These materials exhibit excellent mechanical properties, with easy synthesis conditions favorable for large-scale production [1–6]. These compounds also possess good thermal stability, making them suitable substitutes for diamond in many applications. Outstanding among this class of materials, tungsten tetraboride exhibits superior indentation hardness above 40 GPa under small loads and asymptotic load-independent hardness close to 30 GPa, placing it among the hardest TM-LE compounds [7,8]. Compared to ReB₂, which possesses similarly outstanding mechanical properties [9], tungsten tetraboride holds distinct advantages in its more favorable synthesis requirements and that tungsten is more abundantly available and cheaper than rhenium. Moreover, the mechanical performance of tungsten tetraboride can be improved by alloying with select metals [10].

Despite extensive research on tungsten tetraboride, its crystal structure has long remained unsettled and controversial. Earlier studies [11–13] assigned structures based on limited fitting of x-ray diffraction (XRD) data with reference to related compounds, and also introduced vacancy at metal sites. Recently, there have been extensive theoretical efforts to reexamine previously proposed structures and predict new ones; but all these structures have been found either unstable or incompatible with the stated chemical composition or measured structural and mechanical properties [14–24]. Consequently, no clear consensus has emerged. A major hindrance preventing a definitive resolution of crystal structures of many

TM-LE compounds is the large disparity of XRD signals from electron-poor LE atoms and electron-rich TM atoms. As a result, there is considerable ambiguity in assigning the positions of boron atoms in the crystal structure (Supplemental Material Fig. S1 [25]). To tackle this formidable problem, a recent experimental effort [26] employed neutron diffraction technique that offers a significantly improved resolution of signals from boron atoms relative to those from tungsten atoms, consequently enabling the extraction of insights on key structural features, especially boron trimers occupying vacant tungsten sites in the crystal. There remains, however, major challenges to establish the crystal structure and, equally important, examine its mechanical strengths and elucidate the underlying mechanism.

In this paper we report on structure determination of tungsten tetraboride by a tailored crystal structure search approach that takes into account insights from the recent experiment [26]. The resulting WB_{4.2} phase is in orthorhombic (*Cmcm*) symmetry with a very large 104-atom unit cell, which accommodates key experimental constraints of W:B ratio of 1:4.2, which is the highest boron content tungsten borides can accommodate (thus “highest boride”) [26], and boron trimers occupying vacant tungsten sites. We perform systematic first-principles calculations [25] to assess structural viability and evaluate benchmark mechanical properties. The results indicate that the constructed WB_{4.2} structure exhibits a significantly improved ability to withstand external loading under biaxial indentation strains compared to all previously proposed tungsten tetraboride structures. An analysis of the atomistic deformation modes unveils that boron trimers at vacant tungsten sites play a crucial role in strengthening the crystal under indentation. The present results solve the challenging crystal structure of the highest boride of tungsten, and elucidate the mechanism for its superior indentation strength.

*liquan777@calypso.cn

†chen@physics.unlv.edu

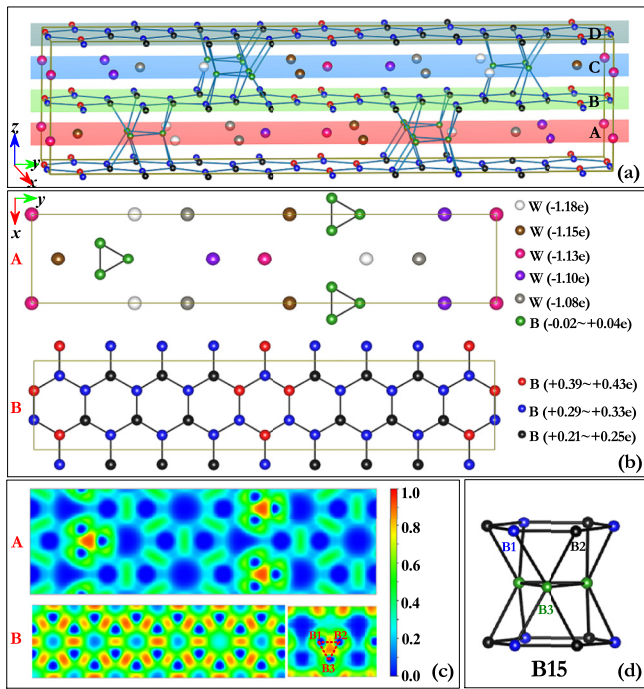


FIG. 1. Crystal structure of *Cmcm* WB_{4.2}. (a) The 104-atom unit cell comprising 20 tungsten and 84 boron atoms, represented by large and small balls, respectively. Boron trimers, shown in green, occupy vacant tungsten sites. The unit cell is divided into four layers, where layers *A* and *B* are related to *C* and *D* by proper symmetry operations. Balls in different colors indicate electron gain or loss by a Bader charge analysis listed in (b), which gives a planar view of atomic arrangements in layers *A* and *B*. (c) Electron localization function in layers *A* and *B*, and the boron trimer in (d), which shows a 15-atom boron tetradecagon, termed B15, comprising a boron trimer connected to two boron hexagons in adjacent layers.

This work advances crystal structure search for materials containing complex multiaatomic constituent units, opening new paths for additional breakthrough discoveries of novel materials and properties.

To search for a viable crystal structure of tungsten tetraboride, we employed the CALYPSO (Crystal structure AnAl-Ysis by Particle Swarm Optimization) method [27,28] combined with first-principles calculations that have been successfully applied to design/clarify the crystal structures of superhard materials for both LE [29] and TM-LE [30] compounds. In this work, we tailored the search to accommodate key constraints set by recent experiment [26], i.e., boron trimers occupying vacant tungsten sites in stoichiometric WB_{4.2}, which restrict the configurational space and facilitates the highly challenging search process. We adopted the Z-matrix method [31] to represent the coherent boron trimer unit during the structural evolution. This process leads to the identification of a WB_{4.2} phase in orthorhombic (*Cmcm*) symmetry with a 104-atom unit cell, comprising 20 tungsten and 84 boron atoms arranged in alternating tungsten and boron layers as shown in Fig. 1(a). The lattice parameters and atomic coordinates for WB_{4.2} are listed in Supplemental Material Table S1 [25]. A prominent feature of this WB_{4.2} phase is that boron trimers replace some tungsten atoms, as suggested by the most recent

experimental probe and analysis [26]. These boron trimers bond to adjacent boron layers, strengthening the crystal under indentation loading, which is in stark contrast to the previously proposed WB_{3+x} model containing interstitial atomic boron atoms that also bond to adjacent boron layers [16], but were shown to cause lattice expansion and weaken the crystal structure, leading to greatly reduced strength in contradiction to the experimentally observed superior indentation hardness [24].

The atomic arrangements in the tungsten and boron layers are shown in Fig. 1(b), along with results on charge states and bonding characters. There is a substantial amount of charge transfer from tungsten to boron, indicating a high degree of ionic nature of the W-B bonds. The electron localization function (ELF) results reveal typical two-centered bonding configurations among the boron atoms in the boron layer; in contrast, there is little net charge gain or loss for boron atoms comprising the trimers, and the ELF results indicate a highly concentrated three-center bonding configuration, which is known to occur in boron polymorphs with significant influence on structural and mechanical properties [32–35]. Each boron trimer occupying a vacant tungsten site connects with boron atoms in adjacent boron layers on both sides to form a 15-atom boron tetradecagon, henceforth referred to as B15 unit, with six triangular and six rectangular faces on the side and capped by two hexagonal faces. Calculated ELF results [Fig. 1(c)] show that each triangular face of the B15 unit also supports a three-center bonding configuration, while boron atoms on the square and hexagonal faces are connected through regular two-center bonds.

The B15 unit is a crucial structural feature of *Cmcm* WB_{4.2}. Recent experimental analysis proposed a model that places two boron trimers directly aligned on the two sides of a hexagonal boron ring to form a cuboctahedron [26]. Our calculations show, however, such a structural arrangement is energetically unfavorable, likely due to the accompanying high stress field in the crystal; instead, each boron trimer prefers to connect to two hexagonal boron rings in adjacent boron layers to form a B15 unit as shown in Fig. 1(a). We have systematically examined boron trimers placed at different locations inside the unit cell, and found that closely packing boron trimers raises the total energy (see details in Fig. S2 [25]). Interestingly, several structural arrangements with different B15 placements exhibit close energetics, suggesting their coexistence that introduces disorder in the distribution of the B15 units in *Cmcm* WB_{4.2}. This result explains the experimental finding that boron trimers in WB_{4.2} do not seem to form an ordered pattern [36].

We have constructed the convex hull of the *Cmcm* WB_{4.2} structure [Fig. 2(a)], taking tungsten metal and α boron as end members, along with various structures identified by the search process [29]; the newly identified WB_{4.2} phase lies extremely close (5 meV/atom) above the convex-hull line. It is known that structures above but close to the convex-hull line often exist as metastable phases, including several tungsten borides [29]. We calculated phonon dispersions of WB_{4.2}, and results [Fig. 2(b)] show no imaginary modes in the Brillouin zone, confirming its dynamic stability. We also have evaluated the Gibbs free energy at finite temperature with configurational entropy contributions from the distribution of the B15

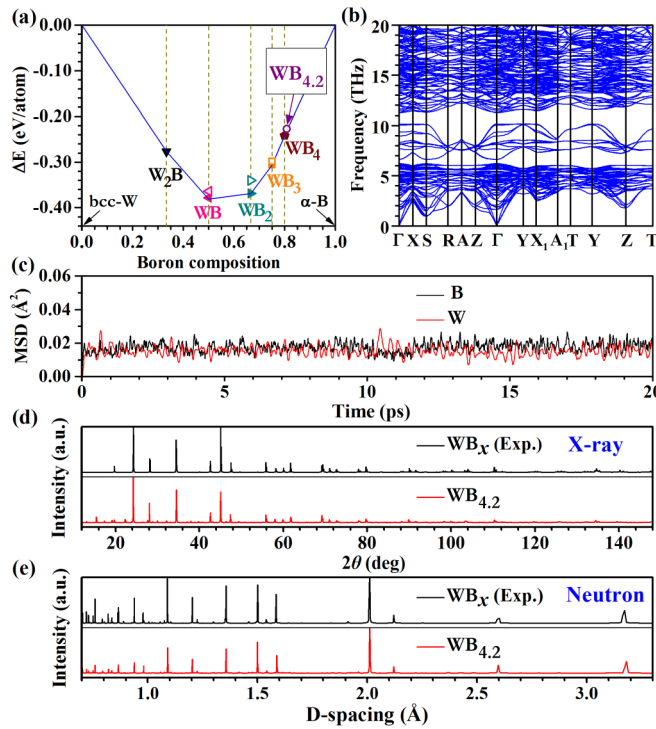


FIG. 2. Structural stability and characterization of *Cmcm* WB_{4.2}. (a) Convex hull where filled (open) symbols represent stable (metastable) structures [29]. (b) Phonon dispersion curves. (c) Mean-squared displacements of atomic positions versus time at 300 K. (d),(e) Simulated XRD and neutron spectra of WB_{4.2} compared to the refined experimental XRD and neutron spectra [26]. X-ray and neutron wavelength are 1.540 56 Å and 1.08 Å, respectively.

units (or boron trimers) in tungsten tetraboride (see Fig. S3 [25] for details). The results show that configurational entropy has a significant effect on stabilizing tungsten tetraboride, making it energetically favorable above 129 K, which is well below the room temperature. We further performed *ab initio* molecular dynamics (AIMD) simulations at 300 K, and the results [Fig. 2(c)] show thermodynamic stability of WB_{4.2} at room temperature.

Our simulated x-ray and neutron diffraction spectra for *Cmcm* WB_{4.2} shown in Figs. 2(d) and 2(e), respectively, agree well with experimental refinement data [26]. Some minor small-angle peaks are present in simulated XRD of WB_{4.2} but absent in refinement data, and these peaks match fine spectral features in raw XRD spectra [26], indicating contributions from boron trimers in a newly constructed WB_{4.2} model. The excellent agreement of simulated neutron spectra of *Cmcm* WB_{4.2} with the refinement data is particularly significant because, as discussed at length in the recent experimental work [26], neutron diffraction better captures contributions from the boron trimers. The present results validate key proposed structural features [26] and establish the first viable structure model for the highest boride of tungsten.

The calculated electronic band structure and density of states of *Cmcm* WB_{4.2} (Fig. S4 [25]) show substantial overlap of the states from tungsten and boron at high binding energies with the Fermi level pinned at the bottom of a pseudogap, which indicate strong bonding between these

states to stabilize and, as will be shown below, strengthen the crystal structure. This is in contrast to the previously proposed WB_{3+x} model with interstitial boron atoms connecting boron layers, where interstitial boron atoms induce bond weakening and structural softening [24]. The distinct structural feature B15 unit in WB_{4.2} plays a key role in stabilizing the crystal by promoting strong W-B bonding while maintaining a strong tetradecagon containing both three-center and two-center boron bonding states. This mixed bonding configuration in a multifaceted structural unit makes B15 much stronger than the planner triangular interlayer bonding by interstitial boron atoms in WB_{3+x}, where the three-center bonding in boron trimers is susceptible to charge transfer and bond breaking [24].

We now examine stress responses of WB_{4.2} crystal to tensile, pure shear, and indentation shear strains to evaluate key structure-property relations, especially the role of the B15 units in influencing benchmark mechanical properties. Calculated stress-strain relations along various major crystallographic directions under these loading conditions are obtained from first-principles calculations and presented in Fig. 3, together with the corresponding structural snapshots right past the lowest stress peaks to assess the dominant bonding variation mechanisms for deformation modes leading to structural failures.

Under tensile loadings, the stress responses along most major crystallographic directions behave similarly, reaching about the same peak stress around 50 GPa, except along the ⟨001⟩ direction where the peak tensile stress is about 20% higher, reaching 61 GPa, due to the enforcement by the extra bonding by the B15 units aligned in the ⟨001⟩ direction, which act as the main load-bearing component in the structure (see Fig. S5 [25] for details in bonding changes). The lowest peak stress among the examined major directions occurs under the ⟨110⟩ strain, perpendicular to the direction of the main bonding network set by the B15 units. The corresponding structural failure is caused by the breakage of boron bonds aligned in the ⟨110⟩ direction away from the B15 units.

When subjected to pure shear loadings, the lowest stress peak among the main slip planes occurs along the deformation path in the ⟨001⟩ plane in the ⟨110⟩ slip direction. Such a behavior is expected for a crystal with quasilayered structural arrangement as in WB_{4.2}, where the interlayer bonding linkage plays the dominant role in setting the strength limit of the crystal. Here the B15 units once again dictate mechanical properties as demonstrated by the stress concentration and resulting elongation of the main load-bearing bonds on the square faces of the B15 units, as shown in Figs. 3(b) and S5 [25].

Indentation loading imposes an additional stress component normal to the sliding shear planes, and the resulting deformation modes change considerably. Under indentation, the elongation of the bonds on the square faces of the B15 units that happens under pure shear is suppressed by the normal stress, because the volume expansion associated with the bond elongation in the normal direction is energetically unfavorable in the presence of the additional indentation compression. We analyze the structural response along the indentation shear deformation path with the lowest peak stress, which sets a lower bound on the ultimate indentation strength of the crystal. Within these constraints, the dominant bond breakage

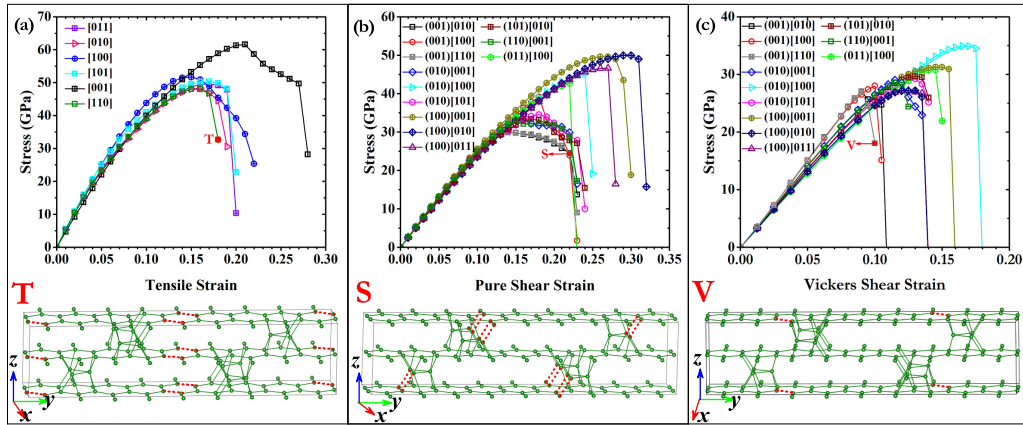


FIG. 3. Stress-strain relations of *Cmcm* WB_{4.2} along major crystallographic directions under (a) tensile, (b) pure shear, and (c) Vickers indentation shear loadings. Also shown are bond-breaking modes in each case along the loading path shortly past the lowest peak stress as indicated on pertinent stress curves. Only the boron atoms in the unit cell are shown for clarity.

leading to structural failure returns to the (001) plane, as in the tensile loading case, as the shear stress component grows; however, the main load-bearing bonds here are located close to the B15 units, aligned in the ⟨110⟩ direction, as shown in Figs. 3(c) and S5 [25]. This indicates shear stress concentration right next to the B15 units, which is reasonable since shear deformation anchors around the bonding structure connecting the relatively shearing layers, while an in-plane tensile deformation would simply pull on all bonds and more extensively stretch the less supported and more vulnerable bonds away from the B15 units.

The mechanical performance of most TM borides is hindered by structure softening under indentation [17,24,34,35], which is rooted in boron's fundamental bonding nature. In boron-rich compounds, boron atoms tend to form quasilayered boron networks, containing both two-center and three-center bonds. The quasilayered bonding and three-center bonds both make the crystal structure vulnerable to deformation and failure by external loading, especially under indentation stresses. Overcoming these constraints is key to improving mechanical properties of TM borides, and the B15 units in WB_{4.2} fulfill such a function by building a strong interlayer connection between adjacent boron layers. The hybrid two-center and three-center bonding in the B15 unit makes it much more capable of withstanding stresses compared to interlayer linkage by single boron atoms that form planar triangular units containing solely three-center bonds as in the previously proposed WB_{3+x} model [22,24]. The WB_{4.2} structure exhibits high indentation strengths along all examined shear slip directions [see Fig. 3(c)] without sharp stress drops caused by unfavorable bonding environments in most TM borides [17,24,34,35]. It is noted that hardness values measured at small loading forces typically scatter widely [8]; meanwhile, asymptotic hardness at large loading forces offers consistent results [3,7,10] that are comparable to calculated indentation strength.

In summary, we have established a viable structure for the highest boride of tungsten WB_{4.2} in orthorhombic (*Cmcm*) symmetry with a very large 104-atom unit cell. Extensive convex-hull, phonon, and AIMD calculations demonstrate that the WB_{4.2} phase is energetically, dynamically, and thermodynamically (meta)stable and satisfies experimentally imposed constraints on composition and key structural features, producing XRD and neutron spectra in excellent agreement with measured data. Our first-principles energetic calculations make a crucial discovery on the key structural unit, B15 tetradecagon, that connects adjacent boron layers, and confirm experimental evidence suggesting that the distribution of boron trimers in WB_{4.2} is likely disordered [26,36]. Our stress-strain calculations under various loading conditions unveil that the B15 units play a decisive role in strengthening the bonding in the crystal and enhancing its ability to generate higher stresses to resist diverse deformations. The present findings of high hardness for WB_{4.2} stemming from the B15 units and the crucial role of the multicenter bonding may open up a new avenue for enhancing the strength and hardness of tungsten borides, and this mechanism is expected to be applicable to other transition-metal borides and other similar materials in a range of stoichiometries [26]. The computational approach developed and results obtained in this work pave the way for rational design and optimization of tungsten tetraboride and related materials, and should stimulate exploration of novel materials hosting multiautomatic structural units and their distinct properties.

We thank Richard B. Kaner for providing refined experimental structural data. This work was supported by the National Key Research and Development Program of China under Grant No. 2018YFA0703404, the Natural Science Foundation of China under Grants No. 11622432, No. 11474125, and No. 11534003, and Program for JLU Science and Technology Innovative Research Team.

[1] E. Gregoryanz, C. Sanloup, M. Somayazulu, J. Badro, G. Fiquet, H. Mao, and R. J. Hemley, *Nat. Mater.* **3**, 294 (2004).

[2] X.-Q. Chen, C. L. Fu, M. Krčmar, and G. S. Painter, *Phys. Rev. Lett.* **100**, 196403 (2008).

- [3] Q. Gu, G. Krauss, and W. Steurer, *Adv. Mater.* **20**, 3620 (2008).
- [4] A. Friedrich, B. Winkler, L. Bayarjargal, W. Morgenroth, E. A. Juarez-Arellano, V. Milman, K. Refson, M. Kunz, and K. Chen, *Phys. Rev. Lett.* **105**, 085504 (2010).
- [5] G. Akopov, M. T. Yeung, C. L. Turner, R. Mohammadi, and R. B. Kaner, *J. Am. Chem. Soc.* **138**, 5714 (2016).
- [6] P. R. Jothi, K. Yubuta, and B. P. T. Fokwa, *Adv. Mater.* **30**, 1704181 (2018).
- [7] R. Mohammadi, A. T. Lech, M. Xie, B. E. Weaver, M. T. Yeung, S. H. Tolbert, and R. B. Kaner, *Proc. Natl. Acad. Sci. USA* **108**, 10958 (2011).
- [8] Q. Li, D. Zhou, W. Zheng, Y. M. Ma, and C. F. Chen, *Phys. Rev. Lett.* **115**, 185502 (2015).
- [9] H. Y. Chung, M. B. Weinberger, J. B. Levine, A. Kavner, J. M. Yang, S. H. Tolbert, and R. B. Kaner, *Science* **316**, 436 (2007).
- [10] R. Mohammadi, M. Xie, A. T. Lech, C. L. Turner, A. Kavner, S. H. Tolbert, and R. B. Kaner, *J. Am. Chem. Soc.* **134**, 20660 (2012).
- [11] A. Chretien and J. Helgorsky, *Compt. Rend. Hebd. Seances Acad. Sci. Colon. (Paris)* **252**, 742 (1961).
- [12] P. Romans and M. P. Krug, *Acta Crystallogr.* **20**, 313 (1966).
- [13] I. Rosenberg and T. Lundström, *J. Solid State Chem.* **6**, 299 (1973).
- [14] M. Wang, Y. Li, T. Cui, Y. Ma, and G. Zou, *Appl. Phys. Lett.* **93**, 101905 (2008).
- [15] E. Zhao, J. Meng, Y. Ma, and Z. Wu, *Phys. Chem. Chem. Phys.* **12**, 13158 (2010).
- [16] Y. Liang, X. Yuan, and W. Zhang, *Phys. Rev. B* **83**, 220102(R) (2011).
- [17] C. Zang, H. Sun, and C. F. Chen, *Phys. Rev. B* **86**, 180101(R) (2012).
- [18] H. Gou, Z. Li, L. Wang, J. Lian, and Y. Wang, *AIP Adv.* **2**, 012171 (2012).
- [19] R. F. Zhang, D. Legut, Z. J. Lin, Y. S. Zhao, H. K. Mao, and S. Veprek, *Phys. Rev. Lett.* **108**, 255502 (2012).
- [20] Y. Liang, Z. Fu, X. Yuan, S. Wang, Z. Zhong, and W. Zhang, *Europhys. Lett.* **98**, 66004 (2012).
- [21] Y. Liang, Y. Gou, Y. Yuan, Z. Zhong, and W. Zhang, *Chem. Phys. Lett.* **580**, 48 (2013).
- [22] X. Cheng, W. Zhang, X. Q. Chen, H. Niu, P. Liu, K. Du, G. Liu, D. Li, H. M. Cheng, H. Ye, and Y. Li, *Appl. Phys. Lett.* **103**, 171903 (2013).
- [23] M. Zhang, H. Yan, Q. Wei, and H. Wang, *Comput. Mater. Sci.* **68**, 371 (2013).
- [24] H. Wu, H. Sun, and C. F. Chen, *Appl. Phys. Lett.* **105**, 211901 (2014).
- [25] See Supplemental Material at <http://link.aps.org/supplemental/10.1103/PhysRevB.100.220102> for details on computational methods and supporting information on stability at finite temperature, XRD analysis, electronic band structure and density of states, representative $WB_{4.2}$ structures with boron trimers substituting at various tungsten sites with corresponding relative energies, and bonding changes near peak stresses under selected key tensile, pure shear, and Vickers shear strains.
- [26] A. T. Lech, C. L. Turner, R. Mohammadi, S. H. Tolbert, and R. B. Kaner, *Proc. Natl. Acad. Sci. USA* **112**, 3223 (2015).
- [27] Y. C. Wang, J. Lv, L. Zhu, and Y. M. Ma, *Phys. Rev. B* **82**, 094116 (2010).
- [28] Y. C. Wang, J. Lv, L. Zhu, and Y. M. Ma, *Comput. Phys. Commun.* **183**, 2063 (2012).
- [29] M. Zhang, H. Y. Liu, Q. Li, B. Gao, Y. C. Wang, H. D. Li, C. F. Chen, and Y. M. Ma, *Phys. Rev. Lett.* **114**, 015502 (2015).
- [30] Q. Li, D. Zhou, W. T. Zheng, Y. M. Ma, and C. F. Chen, *Phys. Rev. Lett.* **110**, 136403 (2013).
- [31] J. Parsons, J. B. Holmes, J. M. Rojas, J. Tsai, and C. E. Strauss, *J. Comput. Chem.* **26**, 1063 (2005).
- [32] H. Tang and S. Ismail-Beigi, *Phys. Rev. Lett.* **99**, 115501 (2007).
- [33] W. Zhou, H. Sun, and C. F. Chen, *Phys. Rev. Lett.* **105**, 215503 (2010).
- [34] C. Zang, H. Sun, J. S. Tse, and C. F. Chen, *Phys. Rev. B* **86**, 014108 (2012).
- [35] B. Li, H. Sun, C. Zang, and C. F. Chen, *Phys. Rev. B* **87**, 174106 (2013).
- [36] E. M. Carnicom, J. Strychalska-Nowak, P. Wisniewski, D. Kaczorowski, W. Xie, T. Klimczuk, and R. J. Cava, *Supercond. Sci. Technol.* **31**, 115005 (2018).

Supplemental Material on
Unravelling the Structure and Strength of the Highest Boride of
Tungsten $\text{WB}_{4.2}$

Weiguang Gong,¹ Chang Liu,¹ Xianqi Song,¹
Quan Li,^{1,2} Yanming Ma,^{1,2} and Changfeng Chen³

¹*State Key Laboratory of Superhard Materials,
Key Laboratory of Automobile Materials of MOE, Department of Materials Science,
and Innovation Center for Computational Physics Method and Software,
Jilin University, Changchun 130012, China*

²*International Center of Future Science,
Jilin University, Changchun 130012, China*

³*Department of Physics and Astronomy,
University of Nevada, Las Vegas, Nevada 89154, USA*

Computational details of first-principles calculations

Density functional theory calculations were performed using the Perdew-Burke-Ernzerh generalized gradient approximation [1] exchange-correlation potential as implemented in VASP code [2]. The electron-ion interaction was described by the all-electron projector augmented-wave method (PAW) [3] with $5d^46s^2$ and $2s^22p^1$ valence electron configurations for W and B atoms, respectively. A plane-wave kinetic energy cutoff of 750 eV and Monkhost-Pack k-mesh with a grid spacing $2\pi \times 0.04 \text{ \AA}^{-1}$ were used for the 104-atom unit cell in the total-energy and stress calculations, with convergence set to 1 meV/atom and $1 \times 10^{-2} \text{ eV/\AA}$, respectively, resulting in residual stresses below 0.1 GPa. The relaxed loading path and ideal strength were determined using an established method [4–7], where at each step the atomic basis vectors and all the strain components orthogonal to the applied stress were simultaneously relaxed. The atomic positions, cell shape, and stress-strain relationships were determined at each quasistatic step by the corresponding relaxation process. Phonon calculations were performed using the direct supercell method as implemented in the phonopy code [8], with forces obtained by the Hellmann-Feynman theorem [9, 10], for a simulation cell containing $2 \times 1 \times 2$ unit cells with a total of 416 atoms. *Ab initio* molecular dynamic (AIMD) simulations were performed on the 104-atom unit cell with a time step of 1 fs at 300 K in an NVT ensemble. We examined electron localization function (ELF) [11, 12] to judge the chemical bonding conditions. The simulated XRD and neutron diffraction patterns are obtained using Reflex modules in Materials Studio. Bader’s Quantum Theory of Atom-In-Molecules analysis was employed to determine charge transfers in the crystal [13–15].

Computational approach for structure prediction

To describe the structural configuration of $\text{WB}_{4.2}$, large unit cells with serious consumption of computing resource are needed in the structural search process. Our preliminary results show that the simulated XRD patterns of the hexagonal $P6_3/mmc-4u$ WB_3 and $P6_3/mmc-4u$ WB_4 with the identical W stacking sequence (sublattice), as well as these modestly defective W sublattices with void sites, that match well with the experimental XRD data of the synthesized tungsten tetraboride ($\text{WB}_{4.2}$) [16, 17], as shown in Fig. S1. These results suggest that the patterns are nearly independent of the occupying positions of boron atoms, stemming from the large atomic scattering cross section ratio of W and B. It is difficult to characterize the specific structural information of B atoms from experiments,

including the atomic coordinates of B trimers, and bonding behaviors. We thus adopted the prior partial structural information from the previously skilled experiments, such as the structural unit of boron trimer and chemical stoichiometry of $\text{WB}_{4.2}$, making it possible to perform structural search by the significant reduction the species of candidates. We thus developed a specially designed search method utilizing structural constraints based on our group developed CALYPSO software to search structures containing void sites or substituted atoms/units.

The generated crystal structures of stoichiometric $\text{WB}_{4.2}$ were based on the superlattices of hexagonal $P6_3/mmc$ -4u WB_3 (up to 6 times of the unit size). The boron trimers and tungsten atoms are randomly distributed on the original tungsten atomic coordinates to achieve the chemical stoichiometry of $\text{WB}_{4.2}$ (e.g., $\text{W}_{10}\text{B}_{42}$ and $\text{W}_{20}\text{B}_{84}$) in the first generation. The Z-matrix method [18] was employed to represent the rigid and rotatable unit of boron trimer, during the structural evolution. In each prediction, the population size in a generation is set to 30, and 30~40 generations are performed in each search process. The proportion of the structures generated by the discrete particle swarm optimization is 60%. When the predicted stable structure is not evolved after five generations, the prediction is considered to reach the criterion of convergence. To search the potential energy landscape sufficiently, several individual predictions have been performed. The use of total energy as the fitness function in the search process guaranteed the search to evolve quickly towards energetically favorable structures. For example, the candidate structures of $\text{W}_{20}\text{B}_{84}$ are designed by the following steps: (i) 6 times superlattices of hexagonal $P6_3/mmc$ -4u WB_3 ($\text{W}_{24}\text{B}_{72}$) are automatically generated (e.g., $2 \times 3 \times 1$, $1 \times 3 \times 2$, $1 \times 2 \times 3$, $1 \times 1 \times 6$ and $6 \times 1 \times 1$); (ii) 4 boron trimers and 20 tungsten atoms are randomly distributed on the original tungsten atomic coordinates in the first generation; and (iii) the proportion of the structures generated by the discrete particle swarm optimization is 60% in the next generations. We eventually confirmed that orthorhombic $Cmcm$ structure with a 104-atom unit cell, comprising 20 tungsten and 84 boron atoms arranged in alternating tungsten and boron layers as shown in Fig. 1(a), is energetically favorable $\text{WB}_{4.2}$ structures over our structure prediction at zero temperature.

Structural stability of $\text{WB}_{4.2}$ at finite temperature

It is known that metastable structures are commonly synthesized, especially among structures above but close to the convex-hull line. Our proposed $\text{WB}_{4.2}$ structure lies extremely

close (5 meV/atom) above the convex-hull line, much lower than the synthesized orthorhombic β -WB (15 meV/atom) and ε -WB₂ (28 meV/atom), and thus is likely to be synthesized in experiment. Furthermore, the tungsten tetraboride was synthesized by arc melting (high-temperature), thus the temperature effect should be taken into account. The distribution of boron trimers in WB_{4.2} is likely disordered as suggested by experimental results and calculated relative energetics. Thus, the role of the configurational and vibrational entropy in free energy should be considered at finite temperature. Our previous calculations [19] show that vibrational entropies of individual units with different structural arrangements tend to balance each other. We therefore have considered the configurational entropy contributions and ignored the vibrational entropy contributions to the free energy at finite temperature for the current tungsten tetraboride. The Gibbs free energy with the consideration of configurational entropy for WB_{4.2} structure is calculated using the following formulas

$$G = U + PV - TS_{conf} \quad (1)$$

Here U, P and V are the DFT total energy, external pressure and crystal, respectively. The third term is the configurational entropy contribution. We evaluated the configurational entropy using

$$S_{conf} = -k_B[x\ln(x) + (1-x)\ln(1-x)] \quad (2)$$

where for the considered WB_{4.2} structure with a 104-atom cell, $x = 1/6$ (4 boron-trimers are distributing at 24 positions of the original tungsten atoms). We present our calculated results in Fig. S3 that provide an assessment of the influence of the configurational entropy contribution to the finite-temperature Gibbs free energy of WB_{4.2}. Our calculations show that the configurational entropy has a significant effect on stabilizing tungsten tetraboride, making it stable above 129 K, which is well below the room temperature.

- [1] J. P. Perdew, K. Burke, and M. Ernzerhof, Phys. Rev. Lett. **77**, 3865 (1996).
- [2] G. Kresse and J. Furthmuller, Phys. Rev. B **54**, 11169 (1996).
- [3] G. Kresse and D. Joubert, Phys. Rev. B **59**, 1758 (1999).
- [4] Y. Zhang, H. Sun, and C. F. Chen, Phys. Rev. Lett. **93**, 195504 (2004).
- [5] Z. C. Pan, H. Sun, and C. F. Chen, Phys. Rev. Lett. **98**, 135505 (2007).
- [6] Z. C. Pan, H. Sun, Y. Zhang, and C. F. Chen, Phys. Rev. B **79**, 104102 (2009).

- [7] Z. C. Pan, H. Sun, and C. F. Chen, Phys. Rev. Lett. **102**, 055503 (2009).
- [8] A. Togo and I. Tanaka, Scr. Mater. **108**, 1 (2015).
- [9] A. Togo, F. Oba, and I. Tanaka, Phys. Rev. B **77**, 184101 (2008).
- [10] A. Togo, F. Oba, and I. Tanaka, Phys. Rev. B **78**, 134106 (2008).
- [11] A. D. Beckeand and K. E. Edgecombe, J. Chem. Phys. **92**, 5397 (1990).
- [12] B. Silviand and A. Savin, Nature (London) **371**, 683 (1994).
- [13] G. Henkelman, A. Arnaldsson, and H. Jonsson, Comput.Mater. Sci. **36**, 354 (2006).
- [14] E. Sanville, S. D. Kenny, R. Smith, and G. Henkelman, J. Comput. Chem. **28**, 899 (2007).
- [15] W. Tang, E. Sanville, and G. Henkelman, J. Phys. Condens. Matter **21**, 084204 (2009).
- [16] A. T. Lech, C. L. Turner, R. Mohammadi, S. H. Tolbert, and R. B. Kaner, Proc. Natl. Acad. Sci. USA **112**, 3223 (2015).
- [17] R. Mohammadi, A. T. Lech, M. Xie, B. E. Weaver, M. T. Yeung, S. H. Tolbert, and R. B. Kaner, Proc. Natl. Acad. Sci. USA **108**, 10958 (2011).
- [18] J. Parsons, J. B. Holmes, J. M. Rojas, J. Tsai, and C. E. Strauss, J. Comput. Chem. **26**, 1063 (2005).
- [19] M. Zhang, H. Y. Liu, Q. Li, B. Gao, Y. C. Wang, H. D. Li, C. F. Chen, and Y. M. Ma,, Phys. Rev. Lett. **114**, 015502 (2015)

TABLE S1: Lattice Parameters and Atomic Coordinates for $\text{WB}_{4.2}$ ($Cmcm$).

Lattice parameters	Wyckoff sites	<i>x</i>	<i>y</i>	<i>z</i>
$a = 5.204 \text{ \AA}$	B1 (16 <i>h</i>)	0.833	0.055	0.998
$b = 27.002 \text{ \AA}$	B2 (16 <i>h</i>)	0.335	0.223	0.006
$c = 6.532 \text{ \AA}$	B3 (16 <i>h</i>)	0.832	0.166	0.002
$\alpha = \beta = \gamma = 90^\circ$	B4 (16 <i>h</i>)	0.330	0.111	0.004
	B5 (8 <i>e</i>)	0.335	0.000	0.000
	B6 (8 <i>g</i>)	0.321	0.147	0.250
	B7 (4 <i>c</i>)	0.500	0.207	0.250
	W1 (4 <i>c</i>)	0.500	0.057	0.250
	W2 (4 <i>c</i>)	0.000	0.111	0.750
	W3 (4 <i>c</i>)	0.000	0.000	0.750
	W4 (4 <i>c</i>)	0.500	0.279	0.750
	W5 (4 <i>c</i>)	0.500	0.166	0.750

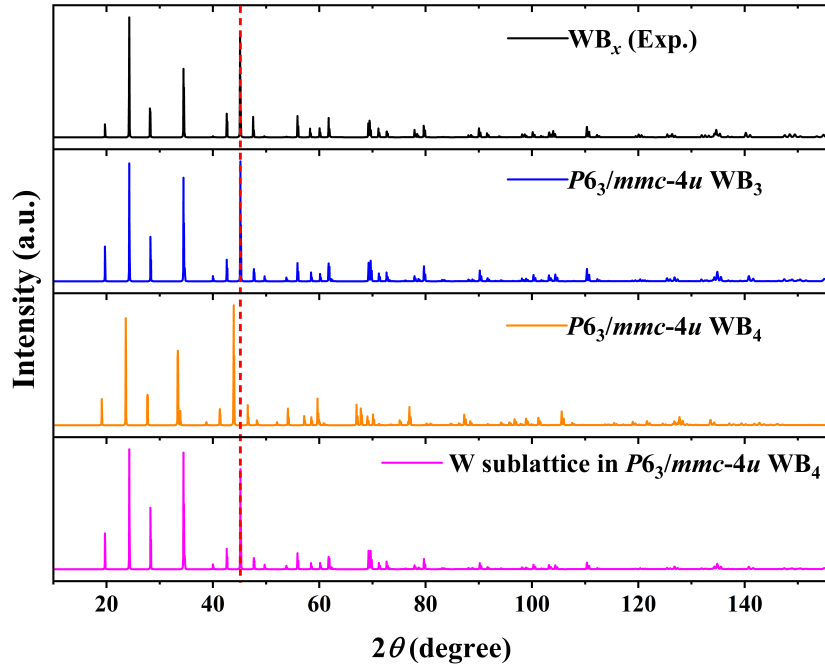


FIG. S1: Simulated XRD patterns of the hexagonal $P6_3/mmc\text{-}4u$ WB_3 , $P6_3/mmc\text{-}4u$ WB_4 and W sublattice in $P6_3/mmc\text{-}4u$ WB_4 , compared to the previously refined experimental data [16]. X-ray wavelength is 1.54056 Å.

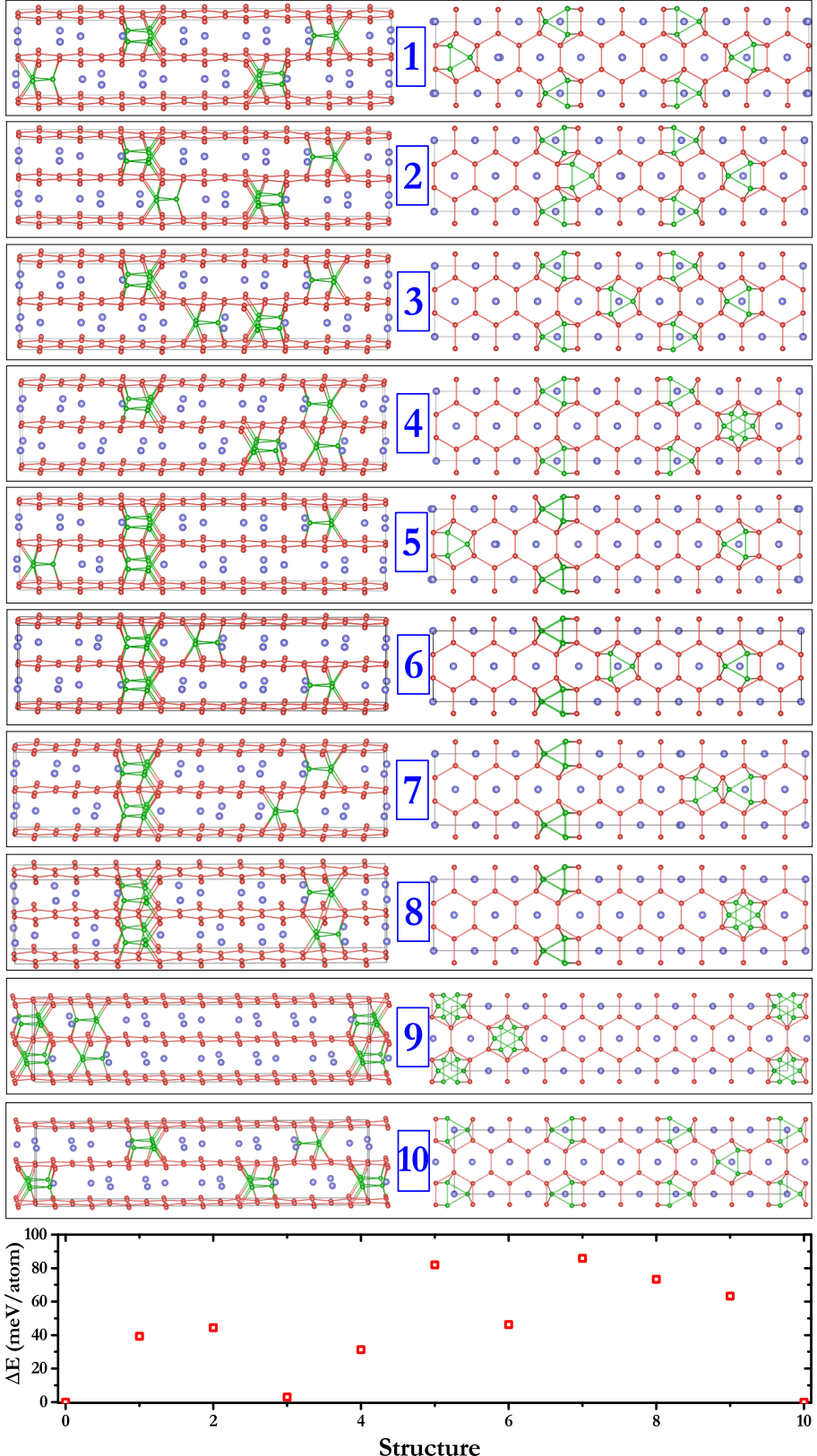


FIG. S2: Representative boron trimer distribution patterns in $\text{WB}_{4.2}$ obtained from a random selection process and the corresponding energies relative to the lowest-energy structure (labeled "0") presented in Fig. 1 of the main text.

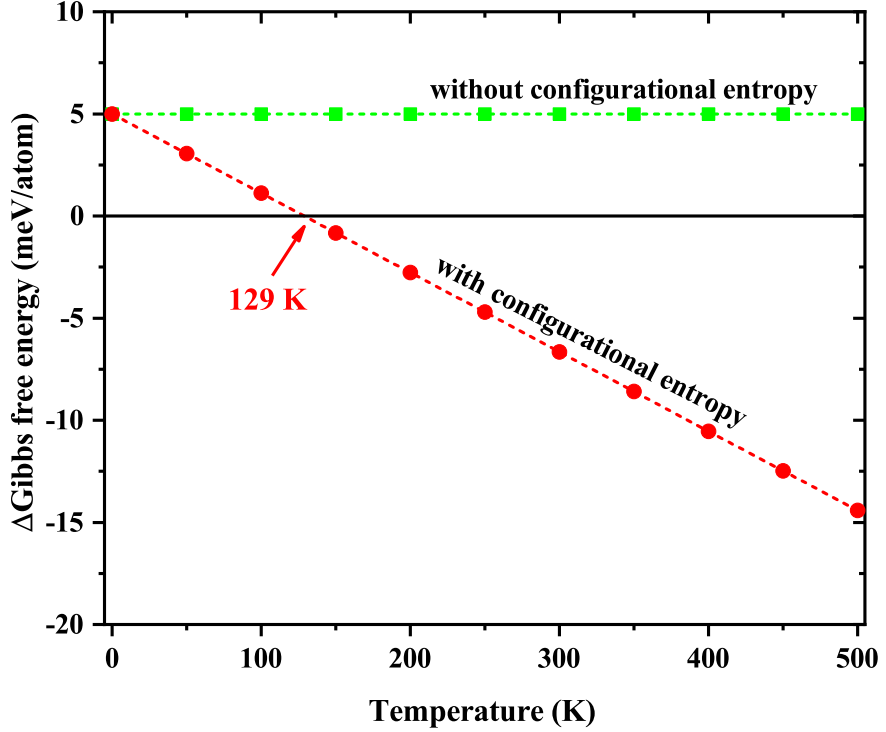


FIG. S3: Calculated Gibbs free energy of the 104-atom $\text{WB}_{4.2}$ structure relative to the convex line as a function of temperature at ambient pressure. Two sets of symbols represent the following results: green squares for results without the configurational entropy contribution, and red circles for results with the configurational entropy contribution.

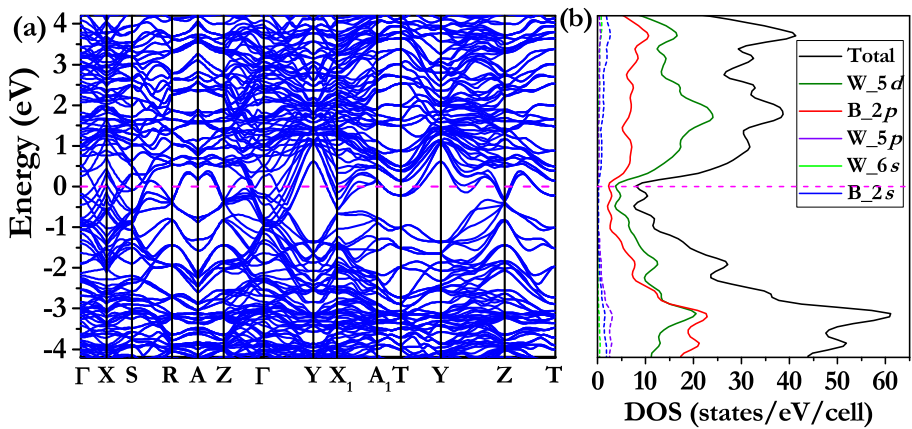


FIG. S4: (a) Electronic band structure and (b) density of states of $Cmcm$ $\text{WB}_{4.2}$.

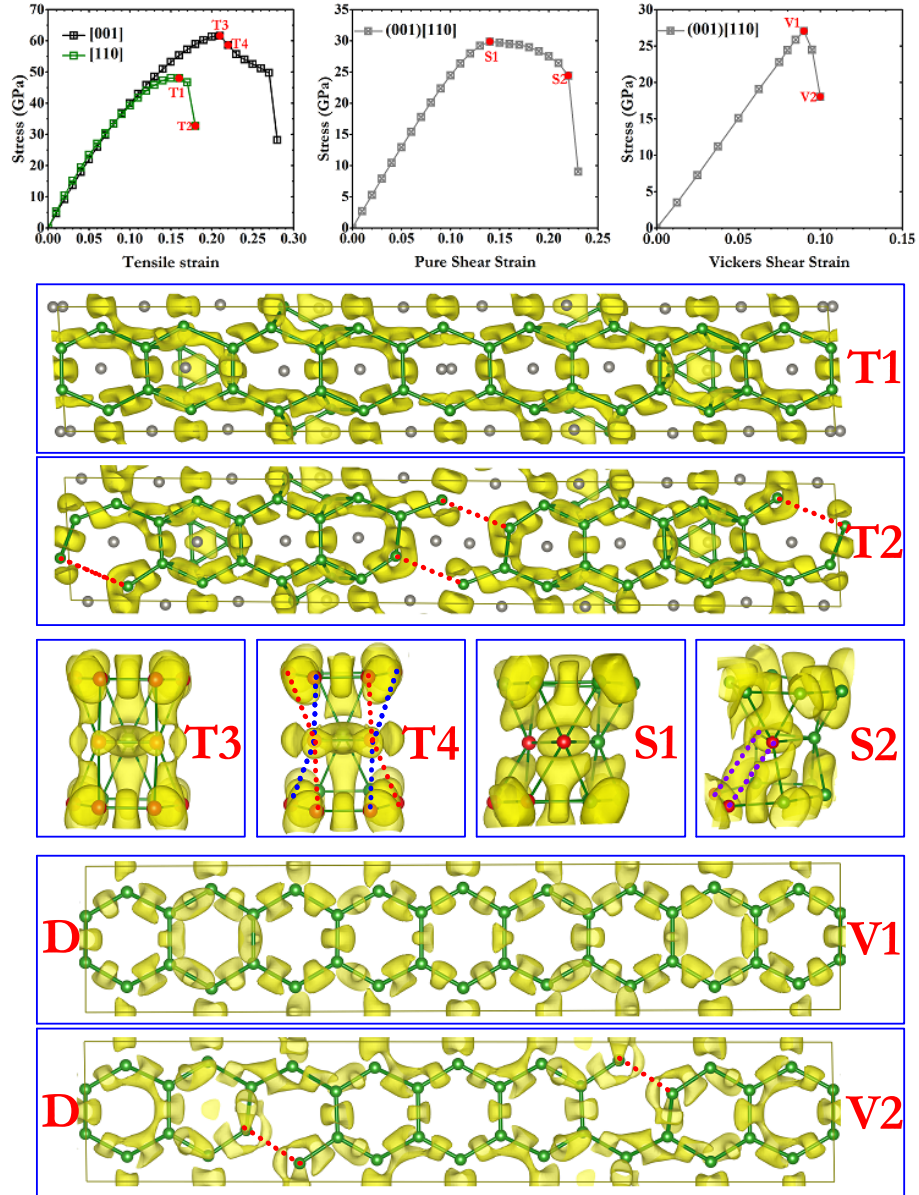


FIG. S5: Detailed bonding changes in $\text{WB}_{4.2}$ as illustrated by the ELF plots at and shortly past the peak stress under select key tensile, pure shear, and Vickers shear deformation modes. Dashed lines in the ELF plots indicate bond breaking patterns under the stated loading conditions.